Strain Measurement in Coronary Arteries Using Intravascular Ultrasound and Deformable Images

Alexander I. Veress
Department of Bioengineering
Department of Radiology
University of Utah
Salt Lake City, UT

Jeffrey A. Weiss[1]
email: jeff.weiss@utah.edu
Department of Bioengineering
University of Utah
Salt Lake City, UT

Grant T. Gullberg
Department of Radiology
University of Utah Medical Center
Salt Lake City, UT

D. Geoffrey Vince
Department of Biomedical Engineering
The Cleveland Clinic Foundation
Cleveland, OH

Richard D. Rabbitt
Department of Bioengineering
University of Utah
Salt Lake City, UT

Atherosclerotic plaque rupture is responsible for the majority of myocardial infarctions and acute coronary syndromes. Rupture is initiated by mechanical failure of the plaque cap, and thus study of the deformation of the plaque in the artery can elucidate the events that lead to myocardial infarction. Intravascular ultrasound (IVUS) provides high resolution in vitro and in vivo cross-sectional images of blood vessels. To extract the deformation field from sequences of IVUS images, a registration process must be performed to correlate material points between image pairs. The objective of this study was to determine the efficacy of an image registration technique termed Warping to determine strains in plaques and coronary arteries from paired IVUS images representing two different states of deformation. The Warping technique uses pointwise differences in pixel intensities between image pairs to generate a distributed body force that acts to deform a finite element model. The strain distribution estimated by image-based Warping showed excellent agreement with a known forward finite element solution, representing the gold standard, from which the displaced image was created. The Warping technique had a low sensitivity to changes in material parameters or material model and had a low dependency on the noise present in the images. The Warping analysis was also able to produce accurate strain distributions when the constitutive model used for the Warping analysis and the forward analysis was different. The results of this study demonstrate that Warping in conjunction with in vivo IVUS imaging will determine the change in the strain distribution resulting from physiological loading and may be useful as a diagnostic tool for predicting the likelihood of plaque rupture through the determination of the relative stiffness of the plaque constituents. [DOI: 10.1115/1.1519279]

Keywords: Strain, Coronary Artery, Soft Tissue Mechanics, Finite Element, Intravascular Ultrasound

Introduction

Coronary heart disease resulted in nearly half a million fatalities in 1996 and is currently the leading cause of death in the United States [1]. The phenomenon of plaque rupture, the structural failure of the plaque cap, is the primary event triggering myocardial infarctions and acute coronary syndromes. Plaque rupture releases thrombogenic lipids and collagen into the blood stream, which subsequently causes thrombus formation [2]. The ability to predict eminent plaque rupture *in vivo* would provide a potential means for selecting patients for interventional therapy.

Stresses in and near the plaque correlate with the location of plaque rupture. Cheng et al. [3] found that 58% of *in vivo* plaque ruptures occurred in the areas of maximum stress, while 83% of failures occurred in high stress areas. Maximum stress levels for eccentric plaques occur at the shoulder area of the cap where the fibrous cap meets the healthy intima [4,5]. Decreased cap thickness causes an increase in the peak shoulder stress when fully developed lipid layers are present [4,6–8]. Clearly, reliable predictions of stress and strain in loaded plaques *in vivo* would provide insight into the potential for subsequent plaque failure. However, the direct measurement of stress during loading of a coronary artery is nearly impossible *in vivo* or *ex vivo*. As an alternative, measurement of strain within the plaque and the wall of the coronary artery can provide insight into the stress distribution.

Intravascular ultrasound (IVUS) uses a catheter-mounted ultrasound transducer to acquire cross-sectional images of an artery with a spatial resolution of 80-100 μm radially and 150-200 μm circumferentially [9,10]. Current IVUS catheters are as small as 0.9 mm and can interrogate most areas of the coronary tree, including coronary arteries in the range of 1.5-5.0 mm in diameter. IVUS provides detailed images of the plaque and vessel wall, both *in vitro* and *in vivo*, thus providing a means to quantify lesion geometry [9–11]. Time sequences of IVUS images contain information about the deformation of both the vessel wall and the plaque. A pointwise correlation between material points in images of the unloaded and loaded artery/plaque system would provide the information necessary to determine strain distributions directly from the IVUS image data.

We have developed and utilized a technique referred to as Warping for strain estimation from sequences of images [12–14]. The technique uses pointwise differences in image pixel intensities between template and target image datasets to generate a distributed body force that deforms a finite element (FE) model of the template so that it registers with the target image. Our ultimate goal is to apply this technique to the study of plaque failure mechanics *in vitro* and *in vivo* by providing information on the biomechanics of atherosclerotic lesions under both physiological loading conditions and loading conditions that arise from interventional procedures such as balloon angioplasty and stent placement. Toward this end, the objectives of the present study were to

[1]Corresponding Author: Jeffrey A. Weiss, Ph.D., Department of Bioengineering, University of Utah, 50 South Central Campus Drive, Room 2480, Salt Lake City, Utah 84112-9202, 801-587-7833.

Contributed by the Bioengineering Division for publication in the JOURNAL OF BIOMECHANICAL ENGINEERING. Manuscript received Aug. 2001. Associate Editor: J. D. Humphrey.

test the efficacy of Warping for determination of strain distributions in plaques from IVUS images by assessing its sensitivity to errors in material model selection, material parameter estimation, and simulated noise in the image data. The hypotheses were that 1) variations in material properties and constitutive model would have a minimal effect on the ability of the Warping technique to predict the strain distribution for an IVUS image registration problem with a known answer for the strain distribution, and 2) the results of Warping IVUS images would be minimally sensitive to noise in the image data.

Materials and Methods

To test the efficacy of Warping for prediction of strains from IVUS images, a pair of IVUS images representing two deformation states of an artery was required. Additionally, the deformation map between the states represented in the images had to be known. To achieve this, a FE model of a diseased coronary artery and plaque was created from an IVUS image of a human left anterior descending coronary artery in an unloaded state obtained during ex vivo imaging. The model was assigned realistic material properties and a physiological pressure was applied to the vessel lumen. FE analysis was performed to determine the strains in the loaded artery and plaque, yielding a ''forward'' FE solution for the strain distribution in the vessel. Using the displacement results from the forward FE analysis, a deformed image (target) was created by applying the displacement map to the original IVUS image (template). Warping analysis was performed using the undeformed and deformed images to produce the forces that deformed the FE mesh. The forward and Warping predictions of strain were compared to determine the accuracy of the technique.

Warping theory. A brief description of the approach for deformable image registration is provided below. A complete description can be found in our previous publications [12,14]. The approach requires an image of the tissue in a reference configuration, referred to as the template, and an image in the deformed configuration, referred to as the target. The Warping technique produces forces from the pointwise intensity differences between the images that act to deform the template image into registration with the target image. An image-based energy density U is defined as the pointwise difference in intensities between the template and target images:

$$U(\boldsymbol{X},\boldsymbol{\varphi})=\frac{\lambda}{2}(T(\boldsymbol{X},\boldsymbol{\varphi})-S(\boldsymbol{X},\boldsymbol{\varphi}))^2. \tag{1}$$

Here, $\boldsymbol{\varphi}(\boldsymbol{X})$ of the deformation map applied to the template image, $\boldsymbol{X}$ represents the reference coordinates of a material point in the template image, T and S are the scalar template and target image intensities at a point in the domain of the deformed template, and λ is a penalty parameter.

The total energy of the continuum, $E(\boldsymbol{\varphi})$, is defined as the sum of the image-based energy density and the standard strain energy density of the material, $W(\boldsymbol{X},\boldsymbol{C})$:

$$E(\boldsymbol{\varphi})=\int_B W(\boldsymbol{X},\boldsymbol{C}(\boldsymbol{\varphi}(\boldsymbol{X})))\,dV+\int_B U(\boldsymbol{X},\boldsymbol{\varphi}(\boldsymbol{X}))dV. \tag{2}$$

Here, $\boldsymbol{C}$ is the right deformation tensor. At equilibrium, the total energy in the system is minimized and the internal forces due to the divergence of the stress tensor balance with the forces that arise from the image-based energy term. The weak form of the momentum equation, with the addition of the influence of the image data, is obtained by taking the first variation of $E(\boldsymbol{\varphi})$ with respect to $\boldsymbol{\varphi}$ [14]. The resulting Euler-Lagrange equations contain the image-based force term:

$$\frac{\partial U}{\partial \boldsymbol{\varphi}}=\lambda(T(\boldsymbol{X},\boldsymbol{\varphi}(\boldsymbol{X}))-S(\boldsymbol{X},\boldsymbol{\varphi}(\boldsymbol{X})))\left(\frac{\partial T}{\partial \boldsymbol{\varphi}}-\frac{\partial S}{\partial \boldsymbol{\varphi}}\right). \tag{3}$$

This vector term is analogous to a position- and deformation-dependent body force that acts to simultaneously minimize local differences in image intensity and intensity gradients between the template (deforming) and target (stationary) images. The image gradients provide the local direction information for the force vector, and the image data do not contribute to the force term when either the local image intensities are equal or the local image intensity gradients are equal.

Constitutive equation. Specification of a particular constitutive model and associated material parameters is required for both the forward FE analysis and the Warping analyses performed in this validation study. For the Warping analyses, the stresses that arise from the constitutive model serve to regularize the otherwise ill-posed problem by providing a force field that opposes the Warping forces, while the continuum mechanics formulation ensures a one-to-one mapping between template and target images. One of the objectives of this work was to assess the sensitivity of Warping strain predictions to variations in material properties, since in most cases of practical interest the actual material properties are unknown. In such cases one must provide an estimate of an appropriate type of material response (e.g., hyperelastic, viscoelastic, with appropriate local material symmetry) along with some estimate of the associated material parameters. To approximate the nonlinear behavior of the arterial wall [15–23] and atherosclerotic lesions [6,24,25], a transversely isotropic hyperelastic strain energy was utilized. The strain energy describes a material that consists of fibers imbedded in an isotropic ground substance:

$$W=F_1(\tilde{I}_1,\tilde{I}_2)+F_2(\tilde{\lambda})+\frac{K}{2}[\ln(J)]^2. \tag{4}$$

Here, F_1 represents the behavior of the ground substance while F_2 represents the behavior of the collagen fibers. The final term controls the bulk behavior of the material. K is the bulk modulus of the material. $\tilde{I}_1$ and $\tilde{I}_2$ are the first and second invariants of the deviatoric right Cauchy deformation tensor $\tilde{\boldsymbol{C}}=\tilde{\boldsymbol{F}}^T\tilde{\boldsymbol{F}}$, where $\boldsymbol{F}=\boldsymbol{F}_{vol}\tilde{\boldsymbol{F}}$, $\boldsymbol{F}_{vol}=J^{1/3}\boldsymbol{1}$, $\tilde{\boldsymbol{F}}=J^{1/3}\boldsymbol{F}$ and $J=\det(\boldsymbol{F})$ [26]. The scalar $\tilde{\lambda}$ is the deviatoric stretch ratio along the local fiber direction $\boldsymbol{a}$, which was oriented circumferentially for the present analyses. Note that as the material approaches the incompressible limit, $J\rightarrow 1$, $\tilde{\lambda}\rightarrow\lambda$ and $\tilde{\boldsymbol{F}}\rightarrow\boldsymbol{F}$. A similar strain energy has been used to model the material behavior of the heart [27,28] and ligaments [29].

A neo-Hookean form was used to represent the ground substance matrix:

$$F_1(\tilde{I}_1)=\mu(\tilde{I}_1-3), \tag{5}$$

Where μ is the shear modulus of the matrix. The stress-stretch behavior for the fiber family was represented as exponential, with no resistance to compressive load:

$$\tilde{\lambda}\frac{\partial F_2}{\partial\tilde{\lambda}}=0,\quad \tilde{\lambda}<1;$$

$$\tilde{\lambda}\frac{\partial F_2}{\partial\tilde{\lambda}}=C_3[\exp(C_4(\tilde{\lambda}-1))-1],\quad \tilde{\lambda}\geq 1. \tag{6}$$

Here, C_3 scales the exponential stresses and C_4 defines the fiber uncrimping rate. A detailed description of a similar constitutive model and its FE implementation can be found in the work of Weiss et al. [26].

Determination of material coefficients. The material coefficients for the arterial wall were required to perform the forward FE analysis, and the coefficients used in the forward analysis were used as starting values for the Warping analyses. The initial material coefficients were determined by a nonlinear least squares fit of the constitutive equation described above to the circumferential stress/strain curves presented in the work of Cox et al. [16]. The Cox data were obtained from inflation testing of excised canine coronary arteries with physiological axial prestretch imposed on the artery. Stress/strain curves and incremental elastic moduli

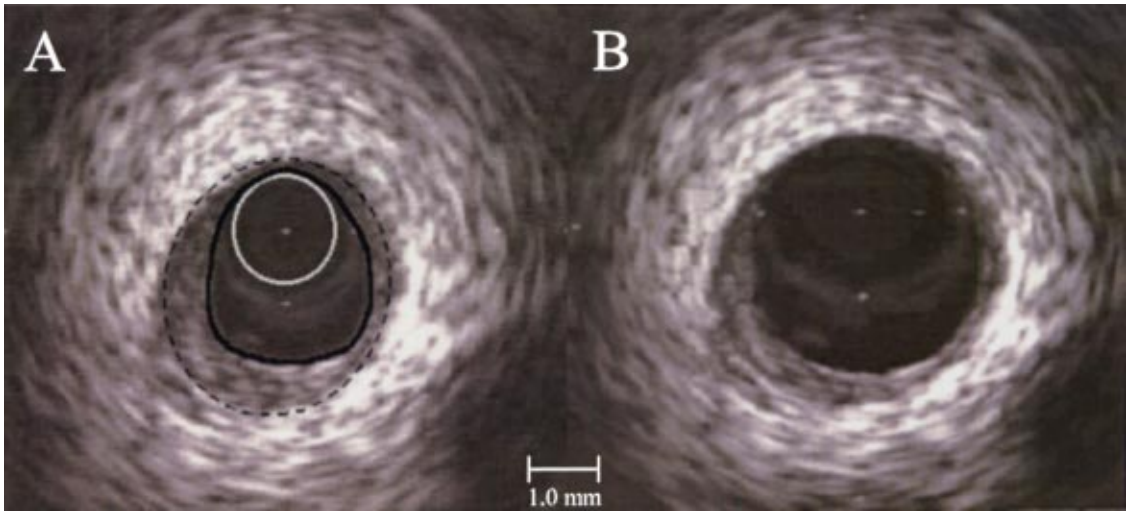

Fig. 1 (*A*) Reference IVUS image of an unloaded ex vivo human left anterior descending (LAD) artery. This image was used as the template in the Warping analyses. The solid white line indicates the IVUS catheter, the solid black line indicates the lumen boundary and the dashed black line indicates the media/adventitia boundary. The target image (*B*) was created by deforming the template image using the deformation map from the forward FE solution (see text for details).

were determined using the method described by Vaishnav et al. [30]. The media/lesion and the adventitia were assigned separate material properties. The media and lesion were defined as a single material due to the lack of material properties for coronary artery plaque. Histological and mechanical testing of aortic plaques have been found to be highly inhomogeneous [6,24,25,31] resulting in material parameter measurements showing large variability. The material coefficients for the media and the lesion were $\mu = 3.57$ Pa, $C_3 = 4.99$ KPa, and $C_4 = 5.49$, while material coefficients for the adventitia were $\mu = 1.97$ KPa, $C_3 = 3.70$ KPa, and $C_4 = 5.49$. The bulk modulus K was 200.00 KPa. As mentioned above, the material properties for the arterial wall/lesion do not need to be exact for this validation analysis because strain results from the forward model were used as the ''gold standard'' in comparisons with the Warping results. The material properties combined with the pressure loading in the forward model need only to produce deformations similar to those found in *ex vivo* experiments. The average lumen strain produced by the forward model was similar to that measured *ex vivo* [32].

Finite element discretization and boundary conditions. The boundaries of the adventitia and media/lesion were manually segmented in the IVUS template image of a diseased vessel (Fig. 1A). Since IVUS cannot distinguish the outer boundary of the adventitia from the connective tissue and fat surrounding the vessel, this boundary was estimated using thickness values found in the literature [33]. B-spline curves were fit to the points generated by segmentation. A 2D plane strain FE model was constructed that included the entire image domain, with the lumen and the tissue surrounding the vessels represented by an isotropic hypoelastic constitutive model with relatively soft elastic material properties ($E = 1.0$ KPa and $\nu = 0.3$) to provide tethering. The outer edges of the image domain were fully constrained to eliminate rigid body motion (Fig. 2A). An internal pressure load of 13.33 KPa (mean arterial pressure of 100 mmHg) was applied to the lumen and a

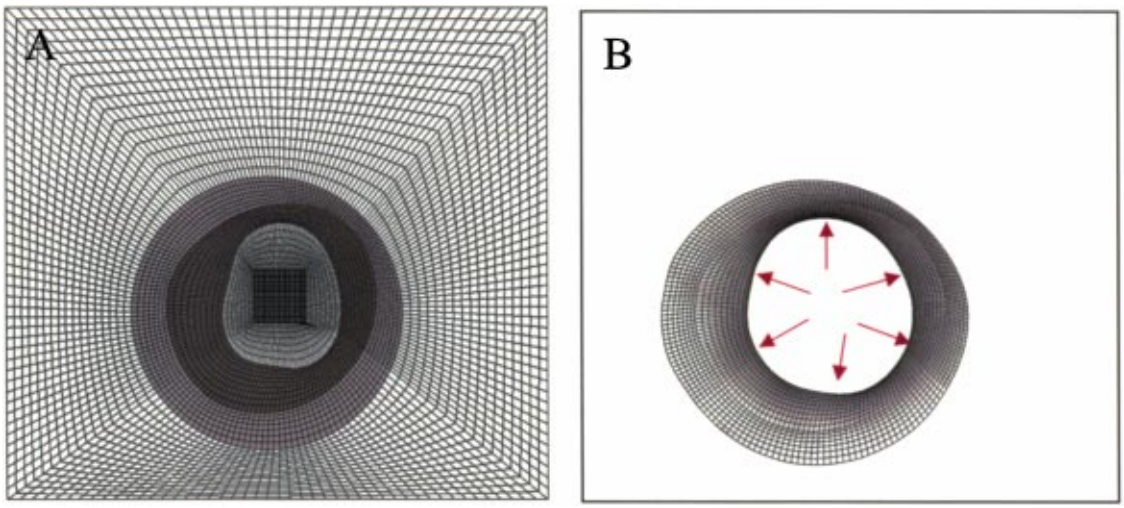

Fig. 2 (*A*) Unloaded finite element mesh; (*B*) Displaced mesh resulting from the internal pressure load imposed on the forward problem. The tether mesh has been removed from the figure for clarity. The pressure loading used in the forward problem is indicated by the arrows.

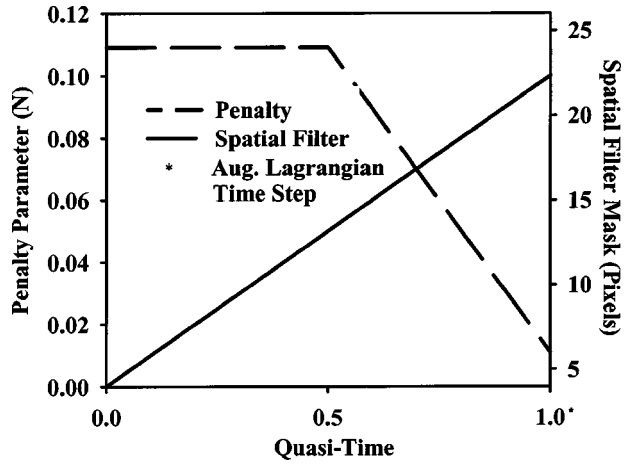

Fig. 3 Changes in spatial filter mask and penalty parameter with computational quasi-time. The penalty was steadily increased over the course of the analysis while the blurring was held constant through the first half of the analysis and then decreased over the second half. The * indicates that the Augmented Lagrangian iterations were completed on the final time step.

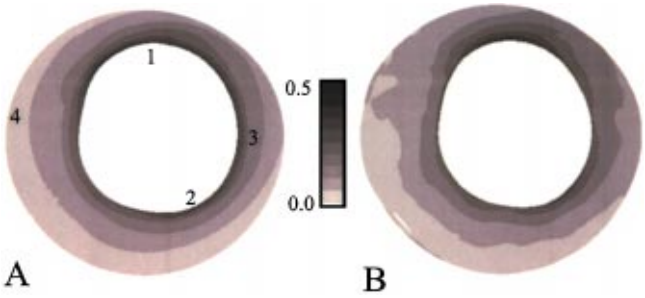

Fig. 4 (*A*) Green-Lagrange 1st Principal strain distribution for the forward problem; (*B*) Strain distribution for the Warping problem. The four comparison locations are shown by their numerical designations.

forward nonlinear FE analysis was performed using NIKE3D [34] (Fig. 2B). Using the displacement fields from the forward FE analysis, the template IVUS image (Fig. 1A) was deformed and resampled onto a regular grid of pixels, yielding a deformed target image for which the exact strains and displacements were known (Fig. 1B). A FE mesh with twice the density of the forward FE mesh was used in Warping analyses to capture local gradients in image intensity. The mesh had a spatial resolution of approximately 240-300 μm radially and 300-400 μm circumferentially. It should be emphasized that the Warping model was not given any internal pressure loading and used only the differences between the template and target IVUS images to deform the FE model of the template image. The fiber stretch and 1st principal strain from the forward and Warping solutions were compared at four locations. Locations 1 and 2 were on the lumen of the lesion in areas of high strain. Location 3 was a mid-wall location that corresponded to the media/adventitia boundary and location 4 was on the outer-wall, corresponding to the outer edge of the adventitia (Fig. 4A).

Sequential spatial filtering. Image registration problems are typically sensitive to local minima. The registration process may get ''stuck'' by alignment of local image inhomogeneities that prevent further image alignment. To avoid this, the algorithm must first register larger image features such as object boundaries and coarse textural detail, followed by registration of fine features. We have circumvented these problems in the present work by employing sequential spatial filtering. By evolving the image sharpness over quasi-time in parallel with or after evolving the penalty parameter, the influence of fine textural features in the image can be minimized until global registration is achieved. The size of the Gaussian mask (number of pixels used in the spatial smoothing convolution [35]) was initially set to 24 pixels and gradually decreased to 6 pixels during the course of the analysis. Both template and target images were filtered for the Warping analyses.

Warping solution procedure. The Warping analysis consisted of three phases (Fig. 3). During the first phase, the penalty parameter λ was gradually increased over quasi-time while the amount of spatial filtering was held constant, providing a means to evolve the image-derived forces on the model and achieve global registration of the deforming template with the target image. In the second phase, the increase in the penalty parameter was continued while the amount of spatial filtering was reduced to facilitate local registration. The final penalty parameter was the largest value that could successfully be used without numerical ill-conditioning affecting the convergence behavior. As a final step in the analysis, an augmented Lagrangian method was used to enforce the image registration constraint. The augmented Lagrangian method allows enforcement of the image alignment constraint to a user-defined tolerance without numerical ill-conditioning, a common problem with the penalty method [36]. Augmentations were continued until a user-defined tolerance was achieved on the change in the L_2 norm of the Lagrange multiplier vector between augmentations. This tolerance was set to 0.03 for all analyses in this validation study, indicating that the change in multipliers was less than 3% between augmentations.

Sensitivity to material coefficients. A parameter study was performed to determine the sensitivity of the Warping predictions of strain to the material coefficients. The Warping solution was performed with 20% increases and decreases in the material coefficients μ and C_3 for the media/lesion portion of the model. For example, the ''μ+20%'' model was run with only the μ coefficient of the media/lesion increased by 20% of the baseline value while the other coefficients for media/lesion and the adventitia were unchanged. The range of variation in the material coefficients was chosen based on the 95% confidence interval of the data used in curve-fitting [16]. The Cox data had an incremental modulus of 1.741$\pm$0.186 KPa ($\pm$ std error) at a pressure load of 125 mmHg, yielding a 95% confidence interval of $\pm$23% of the mean incremental modulus.

*Sensitivity to constitutive model.*To verify that Warping predictions of strain were insensitive to gross errors in selection of constitutive model, the Warping analyses were performed using a neo-Hookean hyperelastic model (rather than a transversely isotropic hyperelastic model) with shear and bulk moduli of μ = 7.00 KPa and K = 500.00 KPa, respectively. The shear modulus was increased and decreased by an order of magnitude and the bulk modulus was decreased one and two orders of magnitude to encompass the variability found in biological tissues. Comparisons were made to strain predictions from the forward FE model with the original transversely isotropic model and material coefficients.

Sensitivity to image noise. IVUS images contain noise. To simulate the effects of noise on image registration using Warping, an independent additive noise model was used to modify the noiseless template and target images [35]. The intensities of the original template and target images were considered true images *s(i,j)*, where *i* and *j* represent pixel coordinates. Random noise *n(i,j)* was added to the true images to create the noisy image *i(i,j)*:

$$i(i,j)=s(i,j)+n(i,j). \tag{7}$$

The noise was defined by the standard deviation (σ_N) of a zero mean normal probability distribution for noise image intensities

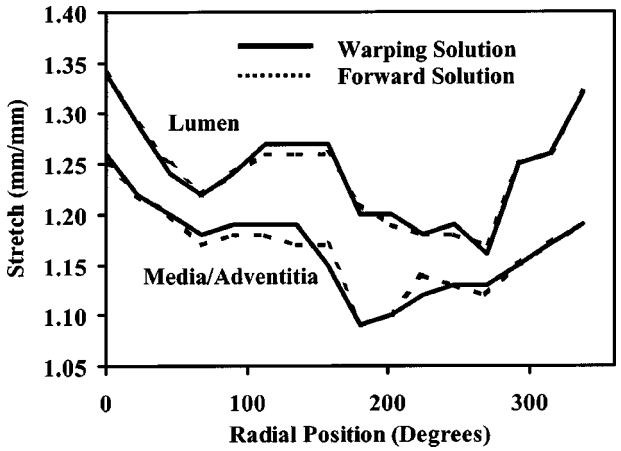

Fig. 5 Circumferential stretch distributions at the lumen and medial/adventitial boundary for the forward and Warping solutions as a function of circumferential location. The forward and Warping stretches at both locations show excellent agreement. The origin is at the 12 o'clock position of the arterial wall and radial position increases in a clockwise manner with respect to the lumen.

[35]. The standard deviations (σ_I) of the image intensities for both the template and target images were 44 gray levels. The signal to noise ratio (SNR) was defined as:

$$SNR = \frac{\sigma_I}{\sigma_N}. \tag{8}$$

SNRs of 8, 4, 1, 0.5 and 0.1 were used (Fig. 6). The strain and displacement fields obtained from the Warping analyses using these SNRs were compared with the results of the forward FE predictions at the four locations described previously.

Results

The Warping strain predictions showed excellent agreement with those of the "exact" forward FE solution (Figs. 4A and 4B). The circumferential stretch distributions at the lumen and at the media/adventitia boundary were nearly identical (Fig. 5). The 1st principal strains were in excellent agreement at all four locations (Table 1) and the circumferential fiber stretches were in excellent agreement at three of the four locations. The largest difference between the forward solution and the Warping solution was at location 4, the outer adventitia, (5% difference for 1st principal strain, 21% for circumferential fiber stretch).

Table 1 Comparison of circumferential fiber stretches/Green-Lagrange 1st Principal strains at four locations between the forward FE solution and the Warping solution.

Location	Forward	Warping	% Difference
1	1.34/0.450	1.33/0.452	3/1
2	1.26/0.320	1.25/0.323	4/1
3	1.09/0.100	1.09/0.101	0/1
4	1.14/0.150	1.11/0.143	21/5

Warping had a low sensitivity to variations in material coefficients of the transversely isotropic hyperelastic model (Table 2). The lesion and arterial wall lumen surface showed the lowest dependence (±0-4% for stretch and ±0-6% for strain), while the mid-wall location and outer-wall location were found to have a higher sensitivity (±0-21% for stretch and ±0-7% for strain).

The substitution of an isotropic constitutive relation for the transversely isotropic relation had little effect on the Warping predictions for both stretch and strain, except as indicated (Table 3). The strains in the lesion and at arterial wall lumen surface showed little dependence on the neo-Hookean material parameters over a range of two orders of magnitude for shear modulus and one order of magnitude for the bulk modulus (±0-9% for stretch and ±0-7% for strain). Lowering the bulk modulus by two orders of magnitude led to larger differences in stretch (±4-32%) and strain (15-20%). The mid-wall location and outer-wall locations were found to have a higher dependence on the bulk modulus (±0-29% for stretch and ±0-27% for strain).

Warping had a low sensitivity to the noise present in the images for SNRs down to 1 (±0-6% for stretch and ±0-9% for strain). Below a SNR of 1 the Warping results showed larger variations with respect to the forward solution answers (Fig. 7) leading to unacceptably large errors. The SNR of 0.1 contained too little image information for the Warping technique to properly deform the FEM mesh, yielding errors of ±60-95% for stretch and ±68-84% for strain.

Table 2 Sensitivity of Warping predictions of circumferential fiber Stretch (λ)/Green-Lagrange 1st Principal Strain (ε) to changes in material parameters. "Forward" refers to results from the forward FE model. Percent differences in stretches/strains are indicated by % Δ. Note that only one parameter (μ or C_3) was varied for any given analysis.

	Forward	μ+20%		μ-20%		C_3+20%		C_3−20%	
Location	λ/ε	λ/ε	% Δ	λ/ε	% Δ	λ/ε	% Δ	λ/ε	% Δ
1	1.34/0.450	1.35/0.450	3/1	1.35/0.430	3/0	1.34/0.453	0/0	1.33/0.450	3/0
2	1.26/0.320	1.26/0.324	0/1	1.27/0.300	4/6	1.26/0.320	0/0	1.25/0.320	4/0
3	1.09/0.100	1.09/0.103	0/3	1.09/0.100	0/0	1.09/0.105	0/5	1.10/0.107	11/7
4	1.14/0.150	1.11/0.140	21/7	1.11/0.141	21/7	1.10/0.150	29/0	1.11/0.146	21/3

Table 3 Sensitivity of Warping predictions of circumferential fiber Stretch (λ)/Green-Lagrange 1st Principal Strain (ε) to changes in material parameters in the isotropic constitutive model. "Forward" refers to results from the forward FE model, while "Base" refers to data obtained using Warping with the same material coefficients as used in the forward FE model. Percent differences in stretches/strains are indicated by % Δ. μ is the shear modulus and K is the bulk modulus. For the base model μ = 7.0 KPa and K=500.00 KPa. Only one parameter was changed at a time for a given analysis.

	Forward	Base		μ=70.0 KPa		μ=0.7 KPa		K=50.0 KPa		K=5.0 KPa	
Loc	λ/ε	λ/ε	% Δ	λ/ε	% Δ	λ/ε	% Δ	λ/ε	% Δ	λ/ε	% Δ
1	1.34/0.450	1.35/0.446	3/1	1.32/0.444	6/2	1.40/0.488	11/2	1.33/0.451	9/1	1.23/0.364	32/20
2	1.26/0.320	1.28/0.330	8/3	1.24/0.300	8/9	1.29/0.335	12/9	1.24/0.330	8/3	1.27/0.367	4/15
3	1.09/0.100	1.09/0.108	0/1	1.09/0.092	0/8	1.09/0.095	0/8	1.09/0.107	0/7	1.12/0.113	14/13
4	1.14/0.150	1.11/0.141	21/6	1.10/0.144	29/4	1.11/0.130	21/13	1.13/0.146	7/3	1.10/0.190	29/27

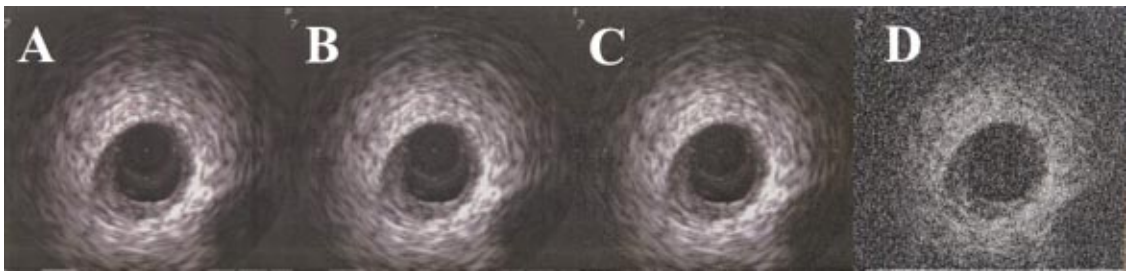

Fig. 6 Effect of increasing levels of additive noise on the appearance of the template image. (*A*) SNR=8, (*B*) SNR=4, (*C*) SNR=1, (*D*) SNR=0.5 and (E) SNR=0.1.

Discussion

The results of this study demonstrate that Warping can reproduce the strain distribution obtained from a forward FE model with little sensitivity to changes in material coefficients and the addition of image noise. Further, the strain distributions predicted by Warping demonstrated little sensitivity to a change in the constitutive model from transversely isotropic to isotropic. Finally, Warping accurately reproduced the strain distribution of the forward FE model even when the shear modulus used in the Warping analyses differed from that of the forward analysis by over two orders of magnitude. This far exceeds the variation in material parameters found in the plaque and arterial wall data reported in the literature [6,15–19,21–24,37,38]. A decrease in the bulk modulus of two orders of magnitude led to unacceptably large differences in both stretch and strain. This value for the bulk modulus is unrealistic for arterial tissue, which is often modeled as nearly incompressible [39,40]. These results indicate that the constitutive representation used with Warping primarily serves to regularize the registration process and ensure a one-to-one mapping [41].

Warping strain predictions were most sensitive to variations in material properties in regions of low image texture and/or contrast. This is likely the reason that the largest errors in strain estimation were found in location 4. This location represents the outer edge of the adventitia, which is the farthest from the IVUS catheter and thus possesses inferior image quality and contrast. Because the Warping forces arise from image intensity differences and their gradients, areas of homogenous intensity (low dynamic range) and/or small intensity gradients generate smaller Warping forces. In these regions, the resistance to deformation is governed by the internal (stress divergence) forces, which in turn depend on material properties and constitutive model. Strains in these regions will be more sensitive to errors in material coefficients and/or choice of constitutive model than in regions with large dynamic ranges and intensity gradients. This observation may provide a means to perform *post hoc* error estimation for future applications, which will be extremely important when Warping is applied to real IVUS image datasets.

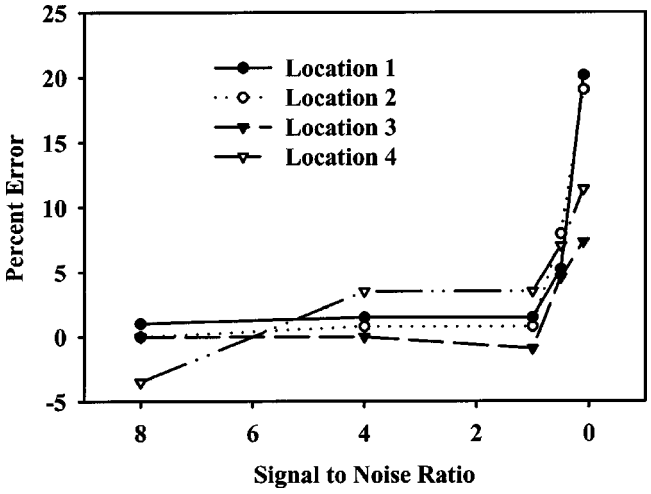

Fig. 7 Effect of SNR on accuracy of strain predictions at the four comparison locations. The strain predictions from Warping were relatively unaffected until the SNR reached a level of 0.1.

Warping was relatively insensitive to image noise. While the noise added to the images was intended to represent detector noise, other types of noise may have different effects on the Warping prediction of strain distributions. For instance, the amount of noise present in IVUS images increases with distance from the transducer. Alternative models of additive noise that take into account spatial position in relation to the catheter would add more noise to data farther from the catheter, further degrading predictions in location 4. This is not likely to affect our planned studies since the plaques are close to the catheter in both the template and target images.

Sampling of the image data onto the Warping FE mesh has important implications for the Warping strain predictions. Image sampling is influenced by both the spatial resolution of the Warping FE mesh and the amount of spatial smoothing. Since the image data are interpolated onto the nodes of the FE mesh, a finer FE mesh improves image sampling. In conjunction with the increased sampling, the spatial smoothing allows for local averaging of the image so that the sampled pixels represent an average of the pixel intensity values within each element. This smoothes sharp intensity gradients, reducing the effects of local minima. In this study, the Warping FE analyses used the same vessel geometry and domain boundaries as the forward FE analysis, but the mesh density was doubled to provide better sampling of the image data. The mask used for spatial smoothing was chosen so that each pixel within a given element represented an average of a neighborhood equal to the smallest element size. These parameters are adjustable and should be optimized for a particular problem class.

Due to the presence of diastolic pressure and residual stress, IVUS images obtained *in vivo* do not provide information regarding the stress-free geometry of the vessel. However, because Warping is insensitive to the constitutive model and material properties, an IVUS image of the vessel during diastole can serve as the template image defining a reference deformation state. The Warping analysis will provide the strain and displacements relative to this reference state. Previous measurements of *in vivo* radial strain distributions for coronary arteries using IVUS have been reported by de Korte et al. [42] and their magnitudes (0.5 to 1.0%) imply that circumferential strains should be readily quantified using the presently described method with similar image resolutions. To determine absolute strain, images of the vessel must be acquired in a completely unloaded state, free of any internal pressure or residual stresses. This would require cutting the vessel wall to relieve residual stresses [43,44] and thus is only feasible for *ex vivo* studies. If the deformation map from the stress-free

state to the intact, passively inflated state were known, the absolute strain state resulting from further loading via inflation or other boundary conditions could be determined [45–48].

The parameter studies used pairs of 2D IVUS images to assess the sensitivity of Warping strain predictions. *In vivo* studies have documented out-of-plane motion as large as 1.5 mm during IVUS image acquisition [49], so clearly 2D images will not be acceptable for monitoring *in vivo* deformations. Full three-dimensional IVUS image datasets obtained using catheter pullbacks can be used to circumvent this difficulty. During the pullback, the catheter is moved through the artery while cross-sectional images are acquired along the length of the vessel. The sequential cross-sectional images can be combined using 3-D reconstruction techniques [50] to create three-dimensional systolic and diastolic image datasets. *Ex vivo* studies do not suffer from out of plane motion, so two-dimensional IVUS image pairs can be used to study the mechanics during *ex vivo* inflation tests.

The results reported herein do not include the predicted stresses in the vessel. Although a Warping analysis also yields the stress distribution within the object, the stresses are only accurate if the material properties and constitutive model for each of the regions of the artery are accurate. There is currently a scarcity of material property data for coronary artery plaques, with the existing data limited to strips of aortic plaque (compression and uniaxial). The acquisition of such data is problematic because plaque samples are highly inhomogeneous [6,24,25,31]. Accurate prediction of stresses using Warping is further complicated by the need for measurement of the internal pressure and the residual stress or strain distribution. IVUS catheters can be retrofitted with pressure transducers to determine diastolic pressure, and the measured pressure can be prescribed to Warping FE models to simulate initial stresses. Thus the potential for estimating stresses using Warping exists but the results would depend on additional approximations and input parameters, especially for the residual stress distribution.

The Warping approach has several advantages over other techniques that determine strain distributions from deformable image registration or correlation. Texture correlation [51,52] suffers from poor accuracy when the angles of rotation associated with the deformation depicted in the images are larger than 8 degrees [53]. Additionally, image pairs with low dynamic range are not effective with texture correlation. Tagged MRI allows the determination of 3-D strain fields [54–56] from pairs of MRI image datasets, but the technique requires long acquisition times that are only feasible for deformations that can be repeated multiple times. Further, tagged MRI has insufficient spatial resolution for use in studies of coronary artery deformation. Speckle tracking has been used to determine the strain in arteries from sequences of images using cross-correlation methods, but large displacements decorrelate the ultrasound images [42,57]. The time delay in the RF signals between IVUS images can be used to determine radial wall strains using cross-correlation methods [37,42,58], but this approach only provides a one-dimensional measure of deformation. Warping does not suffer from any of the above limitations. In particular it can accommodate arbitrarily large, three-dimensional deformations with a spatial resolution approaching that of the image acquisition system.

This study has demonstrated that Warping can be used to accurately determine the strains in a coronary artery using pairs of IVUS images, even in the presence of large errors in material properties and image noise. This provides the foundation for the use of Warping for measurements of strain distributions in arteries relative to a reference configuration, without the need for exact measurements of material properties. By determining strain distributions in coronary artery lesions under static physiological pressure loads and correlating these strain values with the histology of the lesions, insight into the function and interaction of structural components of the plaque under physiological loading. This will provide the basis for studies of balloon angioplasty.

Acknowledgments

Financial support from NIH grants HL39792,CA082813-01A1, AR47369, DC01837 and the Parseghian Foundation is gratefully acknowledged.

References

[1] National Health and Nutrition Examination Survey (NHANES), 1996, CDC/NCHS and the American Heart Association.
[2] MacIsaac, A. I., Thomas, J. D., and Topol E. J., 1993, ''Toward the Quiescent Coronary Plaque,'' J. Am. Coll. Cardiol., **22**, pp. 1228–1241.
[3] Cheng, G. C., Loree, H. M., Kamm, R. D., Fishbein, M. C., and Lee, R. T., 1993, ''Distribution of Circumferential Stress in Ruptured and Stable Atherosclerotic Lesions. A Structural Analysis with Histopathological Correlation,'' Circulation, **87**, pp. 1179–1187.
[4] Loree, H. M., Kamm, R. D., Stringfellow, R. G., and Lee, R. T., 1992, ''Effects of Fibrous Cap Thickness on Peak Circumferential Stress in Model Atherosclerotic Vessels,'' Circ. Res., **71**, pp. 850–858.
[5] Richardson, P. D., Davies, M. J., and Born, G. V., 1989, ''Influence of Plaque Configuration and Stress Distribution on Fissuring of Coronary Atherosclerotic Plaques,'' Lancet, **2**, pp. 941–944.
[6] Loree, H. M., Grodzinsky, A. J., Park, S. Y., Gibson, L. J., and Lee, R. T., 1994, ''Static Circumferential Tangential Modulus of Human Atherosclerotic Tissue,'' J. Biomech., **27**, pp. 195–204.
[7] Veress, A. I., Cornhill, J. F., Herderick, E. E., and Thomas, J. D., 1998, ''Age-Related Development of Atherosclerotic Plaque Stress: A Population-Based Finite-Element Analysis,'' Coron Artery Dis., **9**, pp. 13–19.
[8] Veress, A. I., Vince, D. G., Anderson, P. M., Cornhill, J. F., Herderick, E. E., Klingensmith, J. D., Kuban, B. D., Greenberg, N. L., and Thomas, J. D., 2000, ''Vascular Mechanics of the Coronary Artery,'' Z. Kardiol., **89**, pp. 92–100.
[9] Nissen, S. E., Gurley, J. C., Grines, C. L., Booth, D. C., McClure, R., Berk, M., Fischer, C., and DeMaria, A. N., 1991, ''Intravascular Ultrasound Assessment of Lumen Size and Wall Morphology in Normal Subjects and Patients with Coronary Artery Disease,'' Circulation, **84**, pp. 1087–1099.
[10] Bermejo, J., Botas, J., Garcia, E., Elizaga, J., Osende, J., Soriano, J., Abeytua, M., and Delcan, J. L., 1998, ''Mechanisms of Residual Lumen Stenosis after High-Pressure Stent Implantation: A Quantitative Coronary Angiography and Intravascular Ultrasound Study,'' Circulation, **98**, pp. 112–118.
[11] Hanekamp, C. E., Koolen, J. J., Pijls, N. H., Michels, H. R., and Bonnier, H. J., 1999, ''Comparison of Quantitative Coronary Angiography, Intravascular Ultrasound, and Coronary Pressure Measurement to Assess Optimum Stent Deployment,'' Circulation, **99**, pp. 1015–1021.
[12] Rabbitt, R. D., Weiss, J. A., Christensen, G. E., and Miller, M. I., 1995, ''Mapping of Hyperelastic Deformable Templates Using the Finite Element Method.,'' Proc. SPIE, **2573**, pp. 252–265.
[13] Bowden, A. E., Rabbitt, R. D., and Weiss, J. A., 1998, ''Anatomical Registration and Segmentation by Warping Template Finite Element Models.,'' Proc. SPIE, **3254**, pp. 469–476.
[14] Weiss, J. A., Rabbitt, R. D., and Bowden, A. E., 1998, ''Incorporation of Medical Image Data in Finite Element Models to Track Strain in Soft Tissues,'' Proc. SPIE, **3254**, pp. 477–484.
[15] Cox, R. H., 1975, ''Anisotropic Properties of the Canine Carotid Artery in Vitro,'' J. Biomech., **8**, pp. 293–300.
[16] Cox, R. H., 1978, ''Passive Mechanics and Connective Tissue Composition of Canine Arteries,'' Am. J. Physiol., **234**, pp. H533–541.
[17] Dobrin, P. B., 1986, ''Biaxial Anisotropy of Dog Carotid Artery: Estimation of Circumferential Elastic Modulus,'' J. Biomech., **19**, pp. 351–358.
[18] Dobrin, P. B., and Mrkvicka, R., 1992, ''Estimating the Elastic Modulus of Non-Atherosclerotic Elastic Arteries,'' J. Hypertens. Suppl., **10**, pp. S7–S10.
[19] Dobrin, P. B., and Doyle, J. M., 1970, ''Vascular Smooth Muscle and the Anisotropy of Dog Carotid Artery,'' Circ. Res., **27**, pp. 105–119.
[20] Frobert, O., Gregersen, H., and Bagger, J. P., 1996, ''Mechanics of Porcine Coronary Arteries Ex Vivo Employing Impedance Planimetry: A New Intravascular Technique,'' Ann. Biomed. Eng., **24**, pp. 148–155.
[21] Patel, D. J., and Janicki, J. S., 1970, ''Static Elastic Properties of the Left Coronary Circumflex Artery and the Common Carotid Artery in Dogs,'' Circ. Res., **27**, pp. 149–158.
[22] Patel, D. J., Janicki, J. S., and Carew, T. E., 1969, ''Static Anisotropic Elastic Properties of the Aorta in Living Dogs,'' Circ. Res., **25**, pp. 765–779.
[23] Weizsacker, H. W., Lambert, H., and Pascale, K., 1983, ''Analysis of the Passive Mechanical Properties of Rat Carotid Arteries,'' J. Biomech., **16**, pp. 703–715.
[24] Loree, H. M., Tobias, B. J., Gibson, L. J., Kamm, R. D., Small, D. M., and Lee, R. T., 1994, ''Mechanical Properties of Model Atherosclerotic Lesion Lipid Pools,'' Arterioscler. Thromb., **14**, pp. 230–234.
[25] Salunke, N. V., and Topoleski, L. D., 1997, ''Biomechanics of Atherosclerotic Plaque,'' Crit. Rev. Biomed. Eng., **25**, pp. 243–285.
[26] Weiss, J. A., Maker, B. N., and Govindjee, S., 1996, ''Finite Element Implementation of Incompressible, Transversely Isotropic Hyperelasticity,'' Comput. Methods Appl. Mech. Eng., **135**, pp. 107–128.
[27] Humphrey, J. D., Strumpf, R. K., and Yin, F. C., 1990, ''Determination of a Constitutive Relation for Passive Myocardium: II. Parameter Estimation,'' ASME J. Biomech. Eng., **112**, pp. 340–346.
[28] Humphrey, J. D., Strumpf, R. K., and Yin, F. C., 1990, ''Determination of a

Constitutive Relation for Passive Myocardium: I. A New Functional Form,'' ASME J. Biomech. Eng., **112**, pp. 333–339.
[29] Quapp, K. M., and Weiss, J. A., 1998, ''Material Characterization of Human Medial Collateral Ligament,'' ASME J. Biomech. Eng., **120**, pp. 757–763.
[30] Vaishnav, R. N., Young, J. T., Janicki, J. S., and Patel, D. J., 1972, ''Nonlinear Anisotropic Elastic Properties of the Canine Aorta,'' Biophysics Journal, **12**, pp. 1008–1027.
[31] Salunke, N. V., Topoleski, L. D., Humphrey, J. H., and Mergner, W. J., 2001, ''Compressive Stress-Relaxation of Human Atherosclerotic Plaque,'' J. Biomed. Mater. Res., **55**, pp. 236–241.
[32] Veress, A. I., Bowden, A. E., Vince, D. G., Gullberg, G. T., and Rabbitt, R. D., ''Strain Distribution in Coronary Arteries Determined from IVUS,'' presented at Biomedical Engineering Society Annual Meeting, Seattle, Washington, 2000.
[33] Waller, B. F., Orr, C. M., Slack, J. D., Pinkerton, C. A., Van Tassel, J., and Peters, T., 1992, ''Anatomy, Histology, and Pathology of Coronary Arteries: A Review Relevant to New Interventional and Imaging Techniques—Part I,'' Clinical Cardiology , **15**, pp. 451–457.
[34] Maker, B. N., Ferencz, R. M., and Hallquist, J. O., 1990, ''NIKE3D: A Nonlinear Code for Solid and Structural Mechanics,'' Lawrence Livermore National Laboratories Technical Report UCRL-MA-105208 Rev. 1.
[35] Gonzalez, R. C., and Woods, R. E., 1992, ''Digital Image Processing.'' Addison-Wesley Pub. Co., Reading, Mass., pp. 187–213.
[36] Simo, J. C., and Taylor, R. L., 1991, ''Quasi-Incompressible Finite Elasticity in Principal Stretches. Continuum Basis and Numerical Algorithms,'' Comput. Methods Appl. Mech. Eng., **85**, pp. 273–310.
[37] de Korte, C. L., Woutman, H. A., van der Steen, A. F., Pasterkamp, G., and Cespedes, E. I., 2000, ''Vascular Tissue Characterization with IVUS Elastography,'' Ultrasonics, **38**, pp. 387–390.
[38] Topoleski, L. D., and Salunke, N. V., 2000, ''Mechanical Behavior of Calcified Plaques: A Summary of Compression and Stress-Relaxation Experiments,'' Z. Kardiol., **89**, pp. 85–91.
[39] Chuong, C. J., and Fung, Y. C., 1984, ''Compressibility and Constitutive Equation of Arterial Wall in Radial Compression Experiments,'' J. Biomech., **17**, pp. 35–40.
[40] Carew, T. E., Vaishnav, R. N., and Patel, D. J., 1968, ''Compressibility of the Arterial Wall,'' Circ. Res., **23**, pp. 61–68.
[41] Maintz, J. B., and Viergever, M. A., 1998, ''A Survey of Medical Image Registration,'' Med. Image Anal, **2**, pp. 1–36.
[42] de Korte, C. L., Pasterkamp, G., van der Steen, A. F., Woutman, H. A., and Bom, N., 2000, ''Characterization of Plaque Components with Intravascular Ultrasound Elastography in Human Femoral and Coronary Arteries in Vitro,'' Circulation, **102**, pp. 617–623.
[43] Han, H. C., and Fung, Y. C., 1996, ''Direct Measurement of Transverse Strains in Aorta,'' Am. J. Physiol., **270** (2 pt 2), pp. H750–H759.
[44] Fung, Y. C., and Liu, S. Q., 1992, ''Strain Distribution in Small Blood Vessels with Zero-Stress State Taken into Consideration,'' Am. J. Physiol., **262** (2 pt 2), pp. H544–H552.
[45] Gardiner, J. C., Maker, B. N., and Weiss, J. A., 2001, ''An Iterative Update Algorithm to Enforce Initial Stretch in Hyperelastic Finite Element Models of Soft Tissue,'' presented at Proceedings of ASME Bioengineering Conference.
[46] Lin, I. E., and Taber, L. A., 1995, ''A Model for Stress-Induced Growth in the Developing Heart,'' ASME J. Biomech. Eng., **117**, pp. 343–349.
[47] Taber, L. A., 2000, ''Modeling Heart Development,'' J. Elast. **61**, pp. 165–19.
[48] Weiss, J. A., Maker, B. N., and Schauer, D. A., 1995, ''Treatment of Initial Stress in Hyperelastic Models of Soft Tissues,'' presented at Proceeding of the 1995 Bioengineering Conference, BED-29.
[49] Arbab-Zadeh, A., DeMaria, A. N., Penny, W. F., Russo, R. J., Kimura, B. J., and Bhargava, V., 1999, ''Axial Movement of the Intravascular Ultrasound Probe During the Cardiac Cycle: Implications for Three-Dimensional Reconstruction and Measurements of Coronary Dimensions,'' Am. Heart J., **138**, pp. 865–872.
[50] Cothren, R. M., Shekhar, R., Tuzcu, E. M., Nissen, S. E., Cornhill, J. F., and Vince, D. G., 2000, ''Three-Dimensional Reconstruction of the Coronary Artery Wall by Image Fusion of Intravascular Ultrasound and Bi-Plane Angiography,'' Int. J. Card. Imaging, **16**, pp. 69–85.
[51] Bay, B. K., Yerby, S. A., McLain, R. F., and Toh, E., 1999, ''Measurement of Strain Distributions within Vertebral Body Sections by Texture Correlation,'' Spine, **24**, pp. 10–17.
[52] Bay, B. K., 1995, ''Texture Correlation: A Method for the Measurement of Detailed Strain Distributions within Trabecular Bone,'' J. Orthop. Res. **13**, pp. 258–267.
[53] Chu, T. C., Ranson, W. F., Sutton, M. A., and Peters, W. H., 1985, ''Applications of Digital-Image-Correlation Techniques to Experimental Mechanics,'' Exp. Mech., **25**, pp. 232–244.
[54] McVeigh, E. R., and Bolster, B. D. Jr., 1998, ''Improved Sampling of Myocardial Motion with Variable Separation Tagging,'' Magnetic Resonance in Medicine, **39**, pp. 657–661.
[55] Ozturk, C., and McVeigh, E. R., 2000, ''Four-Dimensional B-Spline Based Motion Analysis of Tagged MR Images: Introduction and in VIVO Validation,'' Phys. Med. Biol., **45**, pp. 1683–1702.
[56] Declerck, J., Feldmar, J., and Ayache, N., 1998, ''Definition of a Four-Dimensional Continuous Planispheric Transformation for the Tracking and the Analysis of Left-Ventricle Motion,'' Med. Image Anal, **2**, pp. 197–213.
[57] Shapo, B. M., Crowe, J. R., Erkamp, R., Emelianov, S. Y., Eberle, M. J., and O'Donnell, M., 1996, ''Strain Imaging of Coronary Arteries with Intraluminal Ultrasound: Experiments on an Inhomogeneous Phantom,'' Ultrasound Imaging, **18**, pp. 173–191.
[58] de Korte, C. L., van der Steen, A. F., Cepedes, E. I., Pasterkamp, G., Carlier, S. G., Mastik, F., Schoneveld, A. H., Serruys, P. W., and Bom, N., 2000, ''Characterization of Plaque Components and Vulnerability with Intravascular Ultrasound Elastography,'' Phys. Med. Biol., **45**, pp. 1465–1475.